Viral nanoparticle vaccines against S100A9 reduce lung tumor seeding and metastasis

Young Hun Chung[a,b] 🆔, Oscar A. Ortega-Rivera[c] 🆔, Britney A. Volckaert[c], Eunkyeong Jung[c], Zhongchao Zhao[b,c], and Nicole F. Steinmetz[a,b,c,d,e,f,g,1] 🆔

Metastatic cancer accounts for 90% of all cancer-related deaths and continues to be one of the toughest challenges in cancer treatment. A growing body of data indicates that S100A9, a major regulator of inflammation, plays a central role in cancer progression and metastasis, particularly in the lungs, where S100A9 forms a premetastatic niche. Thus, we developed a vaccine against S100A9 derived from plant viruses and virus-like particles. Using multiple tumor mouse models, we demonstrate the effectiveness of the S100A9 vaccine candidates in preventing tumor seeding within the lungs and outgrowth of metastatic disease. The elicited antibodies showed high specificity toward S100A9 without cross-reactivity toward S100A8, another member of the S100A family. When tested in metastatic mouse models of breast cancer and melanoma, the vaccines significantly reduced lung tumor nodules after intravenous challenge or postsurgical removal of the primary tumor. Mechanistically, the vaccines reduce the levels of S100A9 within the lungs and sera, thereby increasing the expression of immunostimulatory cytokines with antitumor function [(interleukin) IL-12 and interferonγ] while reducing levels of immunosuppressive cytokines (IL-10 and transforming growth factorβ). This also correlated with decreased myeloid-derived suppressor cell populations within the lungs. This work has wide-ranging impact, as S100A9 is overexpressed in multiple cancers and linked with poor prognosis in cancer patients. The data presented lay the foundation for the development of therapies and vaccines targeting S100A9 to prevent metastasis.

plant virus | bacteriophage | metastasis | S100A9 | vaccine

Advances in radiological and surgical treatment options for localized cancers have greatly reduced the number of deaths in these patients (1). However, novel treatment strategies are urgently needed to treat metastatic diseases, which currently account for 90% of cancer-related deaths (2). Once metastasis has occurred, the 5-y survival rate begins to precipitously drop—this is evidenced in a wide range of cancers including breast (3), melanoma (4), prostate (5), ovarian (6), uterine (6), and cervical cancer (6) among others. Therefore, it is vital that newer therapies and vaccines are developed to slow down or prevent metastatic disease.

The lungs are one of the major organs for metastatic outgrowth, with 20 to 54% of all malignant tumors producing pulmonary metastases (7). One of the key players in lung metastasis is the Ca^{2+}-binding protein S100A9, which forms homo- and heterodimers with S100A8 (8). The S100A8/9 heterodimer exhibits a wide range of functions and is thought to be a major regulator of inflammation (9, 10). It is mostly found in the cytosol of myeloid cells such as macrophages and neutrophils making up more than 45% of the cytosolic content within neutrophils (9).

In cancer and other immune disorders, the S100A8/9 axis becomes dysregulated and causes tumorigenesis and neutrophil necrosis. This leads to additional release of S100A8/9 into the tumor microenvironment (TME), where it interacts with tumor stromal cells and potentiates a positive feedback loop (11, 12). S100A8/9 has been shown to be up-regulated in gastric, esophageal, colon, pancreatic, bladder, ovarian, thyroid, breast cancer, and melanoma (11, 12), and patients with high S100A9 serum concentrations or S100A9+ monocytes have worse prognoses (13–15). Additionally, S100A9 is an early player in tumor proliferation and growth and activates genetic pathways that enhance tumor aggressiveness and metastasis of tumor cells into distant organs (16, 17). S100A9 has further been linked to tumor motility, angiogenesis, and diminished response to immunotherapy and chemotherapeutics (16, 18–21). Importantly, myeloid-derived suppressor cells (MDSCs), which promote an immunosuppressive TME, are directly regulated by S100A8/9 (22). The presence of S100A9 increases MDSC accumulation in both tumor-bearing and naive mice (22, 23). MDSCs also produce and secrete S100A9 themselves and have cognate receptors for S100A9 (24), instigating an autocrine and paracrine feedback loop (22). MDSCs suppress the activity of effector T cells while up-regulating immunosuppressive Tregs. This is achieved through a variety of mechanisms, but cytokines such as transforming growth factor (TGF)β, interleukin (IL)-10, and IL-6 have been implicated (25).

Significance

Metastasis remains one of the toughest challenges in treatment and eradication of cancer. S100A9 is a major regulator of inflammation, and expression is linked with poor prognoses in cancer patients. S100A9 forms a premetastatic niche in lungs recruiting cancer cells and promoting metastasis. Utilizing plant virus and bacteriophage nanotechnologies, we developed a cancer vaccine targeting S100A9. Treatment significantly reduced S100A9 levels within the lungs and sera in tumor-bearing mice protecting from lung metastasis. The vaccines further increased levels of immunostimulatory cytokines and decreased immunosuppressive cytokines. Due to the prevalence of S100A9 in multiple cancer types, we hypothesize that our vaccine could have wide-ranging implications in preventing metastasis.

Within the lungs, S100A8 and S100A9 become up-regulated following distal tumor injection in mice forming a premetastatic niche (26). It was found that S100A8/9 act as indirect chemoattractants and recruit cancer cells by causing the release of TGFβ, tumor necrosis factor α, and vascular endothelial growth factor-A. Neutralizing S100A8 and S100A9 with antibodies helped to block the migration of cancer cells into the lungs, suggesting that active vaccination against S100A9 would be an effective cancer vaccine approach to prevent onset of metastatic disease. Similarly, small-molecule inhibitors of S100A9 such as tasquinimod have been developed and are being tested clinically (27).

While targeting S100A9 has been previously accomplished with silencing RNA (siRNA) (28, 29), neutralizing antibodies (8, 26), and small-molecule inhibitors (27), active vaccination against S100A9 is an advanced approach, which does not require continuous dosing, as the patient produces their own α-S100A9 antibodies. A particular challenge to any "self" vaccine is the need to break tolerance—we achieve this using nanomaterials derived from plant viruses and virus-like particles (VLPs) engineered to display S100A9 peptide epitopes. The nanoparticles thus serve as a display technology and adjuvant. While plant viruses and VLPs are noninfectious toward mammals, they present pathogen-associated molecular patterns, which are recognized by pattern recognition receptors, specifically toll-like receptors, rendering them immunomodulatory and highly effective vaccine technologies (30, 31). They further stimulate immune cells by presenting T helper epitopes (30, 32, 33). Specifically in this work, we utilized the cowpea mosaic virus (CPMV) and Qβ VLP (34–39) to present S100A9 B cell epitopes, which were evaluated in multiple mouse models of triple-negative breast cancer (TNBC) and melanoma.

Results and Discussion

Production and Characterization of S100A9 Vaccine Candidates. A recent study reported an S100A9 vaccine targeting the C terminus of S100A9 $_{104}$GHSHGKGCGK$_{113}$ (40). We modified the vaccine ($_{101}$RGHGHSHGKG$_{110}$) to improve the sequence to be above the 0.5 threshold for a B cell epitope according to the BepiPred-2.0 Sequential B Cell Epitope Predictor (41) (Fig. 1A). Extensive biochemical characterization has confirmed that murine S100A9 is functionally equivalent to its human counterpart (42) with sequence similarity and identity of 79 and 62%, respectively (following NCBI Blast alignment of GenBank peptide sequences of CAC14292 and NP_002956 of mouse and human S100A9, respectively). Nevertheless, amino acid differences in the peptide may require optimization for human clinical translation. We additionally add a GSG linker to the peptide to improve peptide flexibility and thereby peptide conjugation efficiency (43). The GSG linker solely acts as a linking unit and does not impact the function of the peptide (44).

To create the S100A9 vaccine candidates, CPMV was harvested from black-eyed pea No. 5 plants, and Qβ VLPs were expressed in BI21 (DE3) *Escherichia coli* as previously reported (38, 45). CPMV and Qβ present solvent-exposed surface lysines (Lys) (300 per CPMV and 720 per Qβ VLP), which are conjugated to an SM(PEG)$_8$ linker followed by conjugation to the cysteine-terminated S100A9 peptide (Fig. 1B) (46, 47).

Vaccine conjugates denoted as CPMV-S100A9 and Qβ-S100A9 were purified and characterized by ultraviolet-visible spectroscopy (UV-VIS) (*SI Appendix*, Fig. S1A) or the bicinchoninic acid assay to determine their concentration and purity. The yields following conjugation and purification were ~50% of starting material. To confirm
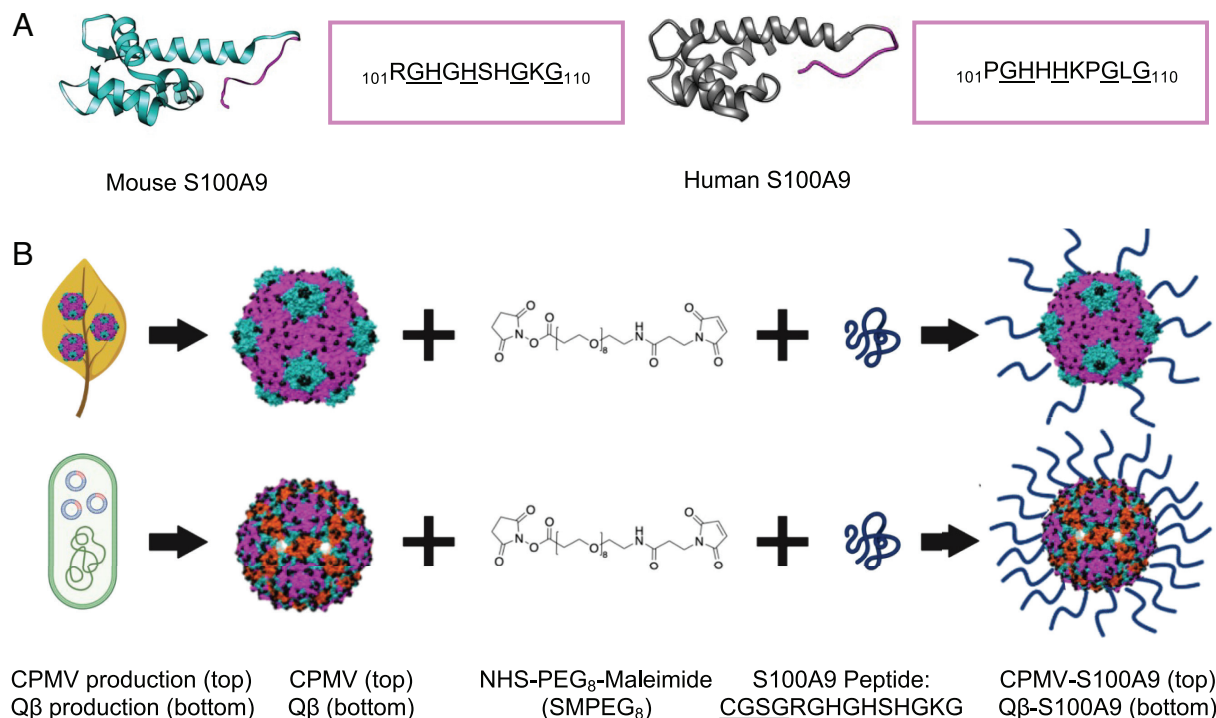
Fig. 1. S100A9 peptide epitope and its conjugation to CPMV and Qβ. (A) Structure of S100A9 and peptide epitope sequence of the S100A9 epitope in mice compared to humans. The identical sequences are underlined. (B) CPMV is produced through mechanical inoculation of black-eyed pea No. 5 plants while Qβ VLPs are expressed in *E. coli*. An SM(PEG)$_8$ linker is conjugated to lysines (shown by black spheres) on the exterior of the viral capsids followed by maleimide coupling of the cysteine-terminating S100A9 peptide. The added CGSG linker is underlined. Qβ contains more surface-exposed Lys (720 vs. 300 for CPMV), which allows for greater peptide conjugation. The figures were drawn on Biorender.com. The structures of the mouse and human S100A9, CPMV, and Qβ were created on Chimera (mouse S100A9 PDB ID: 6DS2, human S100A9 PDB ID: 6ZDY, CPMV PDB ID: 1NY7, Qβ PDB ID: 1QBE), and the SM(PEG)$_8$ chemical structure was drawn on ChemDraw. The small (fivefold axis) and large (twofold and threefold axis) CP of CPMV are shown in green and pink, respectively, and for Qβ CPs are pictured in pink, green, and red according to their symmetry (5-3-2 fold axis, respectively). CPMV has pseudo-T3 and Qβ has T3 symmetry.

structural integrity and epitope display, native gel electrophoresis (*SI Appendix*, Fig. S1*B*) as well as sodium dodecyl sulfate–polyacrylamide gel electrophoresis (SDS-PAGE, *SI Appendix,* Fig. S1*C*) were performed. While CPMV-S100A9 had reduced electrophoretic mobility vs. CPMV, Qβ-S100A9 showed increased mobility vs. Qβ. In both the CPMV and Qβ gels, the RNA and protein colocalize, indicating that stable and intact conjugates were obtained. While Qβ is a VLP, it packages host RNA, which is visualized by the GelRed stain (48). SDS-PAGE demonstrated conjugation of ~120 peptides per Qβ and ~30 peptides per CPMV (*SI Appendix,* Fig. S1*C*), consistent with a higher density of surface Lys per Qβ vs. CPMV (46, 47). CPMV consists of 60 copies each of two coat proteins (CPs), a large (L) CP of 42 kDa and a small (S) CP of 24 kDa (*SI Appendix,* Fig. S1*C*, red boxes). The secondary, higher-molecular-weight band above the native CP bands (e.g., S CP-S100A9 or L CP-S100A9 as well as Qβ CP) is in agreement with coupling of the S100A9 peptide, which has a molecular weight of 1.33 kDa (including the linker). Quantification of peptide per nanoparticle and ratio of CP-S100A9 vs. free CP was carried out using densitometry analysis and ImageJ software (https://imagej.nih.gov/ij/download.html) to analyze the ratio of CP-S100A9 vs. free CP.

Transmission electron microscopy (TEM), dynamic light scattering (DLS), and size exclusion chromatography (SEC) using fast protein liquid chromatography of the vaccine candidates confirmed the presence of intact particles (*SI Appendix,* Fig. S1 *D–F*). The TEM images showed monodisperse and intact nanoparticles with similar size and morphology to the native particles (*SI Appendix,* Fig. S2*A*). The DLS data and SEC analysis corroborate these results (*SI Appendix,* Figs. S1 *E* and *F* and S2 *B* and *C*). The elution profiles of CPMV-S100A9 and CPMV were similar around 11 mL and an A260:280 ratio of 1.8, indicating intact particles (*SI Appendix,* Figs. S1*F* and S2*C*). For the Qβ-S100A9 sample, the size did increase after conjugation with ~32.7 for Qβ and ~42.7 nm for Qβ-S100A9 as well as elution profiles of 8.7 mL for Qβ-S100A9 vs. 11.8 mL for Qβ (*SI Appendix,* Figs. S1 *E* and *F* and S2 *B* and *C*).

Immunization with CPMV-S100A9 and Qβ-S100A9 Vaccine Candidates. C57BL/6J mice were vaccinated 3× spaced 2 wk apart (Fig. 2*A*). The CPMV-S100A9 and Qβ-S100A9 vaccines were injected subcutaneously (s.c.) at 200 µg per dose along with negative controls of PBS, CPMV, Qβ, and the S100A9 peptide (free S100A9 dose was equilibrated to the Qβ-S100A9 sample as the Qβ-S100A9 sample contained 4× more peptide than CPMV-S100A9). Pre- and postimmunization bleeds were collected, and 2 wk after the last boost, tumor challenge was performed (see below). Both CPMV-S100A9 and Qβ-S100A9 elicited significant antibody titers against the S100A9 peptide, as measured through the enzyme-linked immunosorbent assay (ELISA) (Fig. 2*B*). CPMV-S100A9 endpoint titers peaked at week 6 at 25,600, while Qβ-S100A9 end point titers remained consistent from weeks 4 to 8 ranging from 800,000 to 880,000. The higher antibody titers of the Qβ-S100A9 vs. CPMV-S100A9 are explained by the higher density of labeling of Qβ-S100A9. As expected, the control groups did not yield any S100A9-specific antibodies. Importantly, the lack of antibody production by the peptide group demonstrates that peptide vaccination is ineffective and that a necessary adjuvant and carrier such as with CPMV or Qβ is necessary. We further investigated the IgG isotypes. A ratio of IgG2b IgG1^{-1} > 1 was deemed as a Th1 bias, while a ratio <1 was deemed to be Th2-biased (49). In the C57BL/6J mice, we saw opposing trends in the isotyping patterns between the vaccines (Fig. 2*C*). While CPMV-S100A9 originally started with a Th2 bias, by week 6, the bias began to skew strongly toward Th1. The strong delineation toward a Th1 bias may be due to the adjuvant

nature of CPMV—CPMV leads to upregulation of Th1 cytokines such as interferon (IFN)γ (50). On the other hand, vaccination with Qβ-S100A9 started Th1 but appeared balanced starting from week 4. Because C57BL/6J mice also produce IgG2c antibodies, the ratio of IgG2c to IgG1 was also investigated, but IgG2c antibodies were not produced with either vaccine (Fig. 2*C*).

Mice immunizations were repeated in BALB/C mice. The CPMV-S100A9 group did not elicit significant antibody titers (*SI Appendix,* Fig. S3); in contrast, Qβ-S100A9 produced strong titers starting from week 2 (Fig. 2*D*). Immune responses in BALB/C are Th2-biased, while C57BL/6J exhibit Th1 bias (51). CPMV is known to induce a strong Th1 response; therefore, as an adjuvant, it may not be as potent in the Th2-biased BALB/C mice. The isotyping was repeated in the BALB/C mice with the Qβ-S100A9 formulation (Fig. 2*E*). The Qβ-S100A9 initially produced a Th1 bias and then regressed to a balanced response as in the C57BL/6J mice (Fig. 2 *C* and *E*). BALB/C mice produce IgG2a antibodies, so the IgG2a IgG1^{-1} ratio was determined and showed similar trends—starting with a Th1 bias and then shifting toward a balanced response. Last, IgM antibodies were measurable in both vaccine groups in BALB/C and C57BL/6J mice, but IgE was not apparent (*SI Appendix,* Fig. S4*A*). IgA was detectable in small quantities in BALB/C mice only for the Qβ-S100A9 group (*SI Appendix,* Fig. S4*B*). The immunization with CPMV/Qβ-S100A9 elicited high antibody titers. The viral nanoparticles (VNPs) act as a carrier and adjuvant, and recent research highlights that in particular, conjugation results in codelivery of the epitope and adjuvant to the same cell boosting the potency of antibody production (52–55).

Antibody production against the CPMV and Qβ was also measured (*SI Appendix,* Figs. S5 and S6). In BALB/C and C57BL/6J mice, the Qβ endpoint titers were at 25,600 and 409,600 for all timepoints, respectively, which were the last dilutions tested (*SI Appendix,* Fig. S5 *A* and *B*). We expected antibodies against the carrier, and data suggest that the presence of α-carrier antibodies does not impair vaccine efficacy (35). In fact, the presence of α-carrier antibodies may boost efficacy—for example, in ongoing trials with a Qβ-based in situ immunotherapy, patients are preimmunized with Qβ VLPs to stimulate α-Qβ antibody production, which enhances APC uptake and targeting (56–58). CPMV and CPMV-S100A9 also induced potent antibody production against the CPMV VNP capsid (*SI Appendix,* Fig. S6). At week 2, they both had average endpoint titers of 19,200, while at weeks 4 to 8, they both had endpoint titers of 25,600, the last measured dilution (*SI Appendix,* Fig. S6). Next, western blots (WBs) and dot blots (DBs) were performed to validate whether antibodies produced recognize full-length S100A9 protein (denatured or native, respectively). WBs and DBs did indeed confirm binding to S100A9 with no cross-reactivity against another member of the S100A family, S100A8 (*SI Appendix,* Fig. S7).

CPMV- and Qβ-S100A9 Vaccines Decrease Tumor Seeding within the Lungs of Melanoma and TNBC. To assess the effectiveness of the vaccines in preventing metastasis, we started with i.v. (intravenously) models of B16F10 melanoma and 4T1-Luc TNBC. While these models are not perfect indicators of metastasis, they can be used as tumor-seeding models within the lungs. We vaccinated both C57BL/6J and BALB/C mice prior to B16F10 and 4T1-Luc injection (Fig. 3 *A* and *D*) simulating vaccination postsurgery before the seeding of metastatic nodules within the lungs. Three weeks post-B16F10 challenge (using 50,000 cells), the lungs were harvested and tumor nodules were manually counted. Compared to the control groups (CPMV, PBS, and free S100A9 peptide), the CPMV-S100A9 vaccine led to a 10.7-, 9.7-, and 7.6-fold reduction in tumor nodules, respectively (Fig. 3 *B*, *Left*).
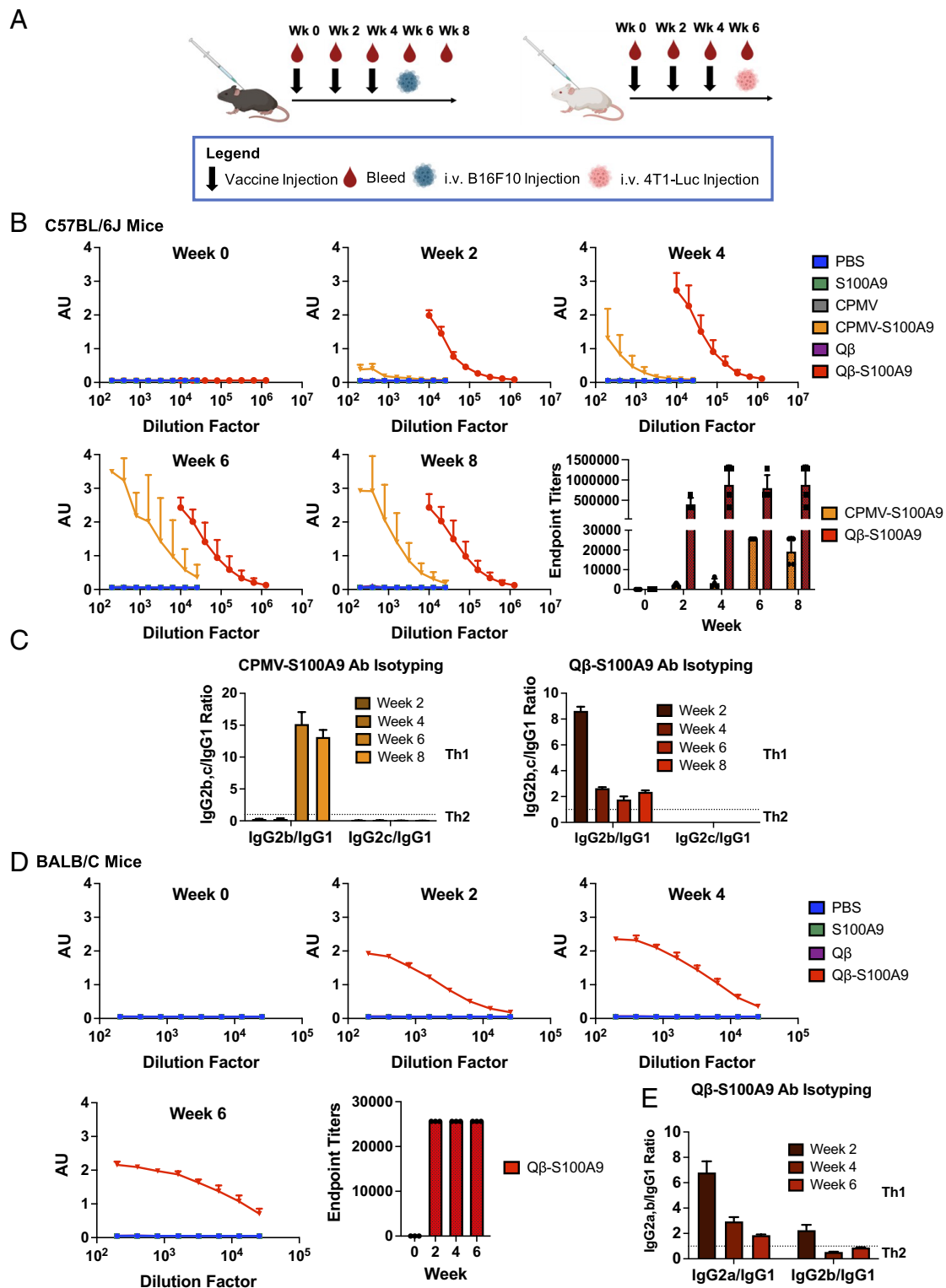
Fig. 2. Antibody titers against the S100A9 epitope following vaccination of mice. (*A*) Vaccine injection schedule in both C57BL/6J (*Left*) and BALB/C (*Right*) mice. The vaccine candidates were given in a prime and double boost spaced 2 wk apart. Tumor burden is shown in Fig. 3. (*B*) Titers against the S100A9 peptide in C57BL/6J mice (n = 3 to 4). The endpoint titers were determined as the titer range at which the absorbance was twice the absorbance of the blank. (*C*) IgG Isotyping of the CPMV and Qβ-S100A9 vaccines in C57BL/6J mice. (*D*) Titer production and endpoint titers against the S100A9 peptide in BALB/C mice (n = 2 to 3). (*E*) IgG isotyping of the Qβ-S100A9 vaccines in BALB/C mice. The injection schedule schematics were created on Biorender.com. The error bars represent the SD.

With the Qβ-S100A9 vaccine, there was a 4.5-, 6.6-, and 5.1-fold reduction in tumor nodules compared to Qβ, PBS, and the S100A9 peptide, respectively (Fig. 3 *B*, *Left*). It is of note that there was no significant difference between the Qβ-S100A9 and CPMV-S100A9 vaccines, which may indicate that a threshold of effective titers was achieved and that a lesser dose of Qβ-S100A9 may be sufficient. We further validated vaccine efficacy by injecting 100,000 (vs. 50,000) B16F10 melanoma cells and harvesting the lungs after 2 wk—again, potent efficacy was demonstrated (Fig. 3 *B*, *Right*, Fig. 3*C*).
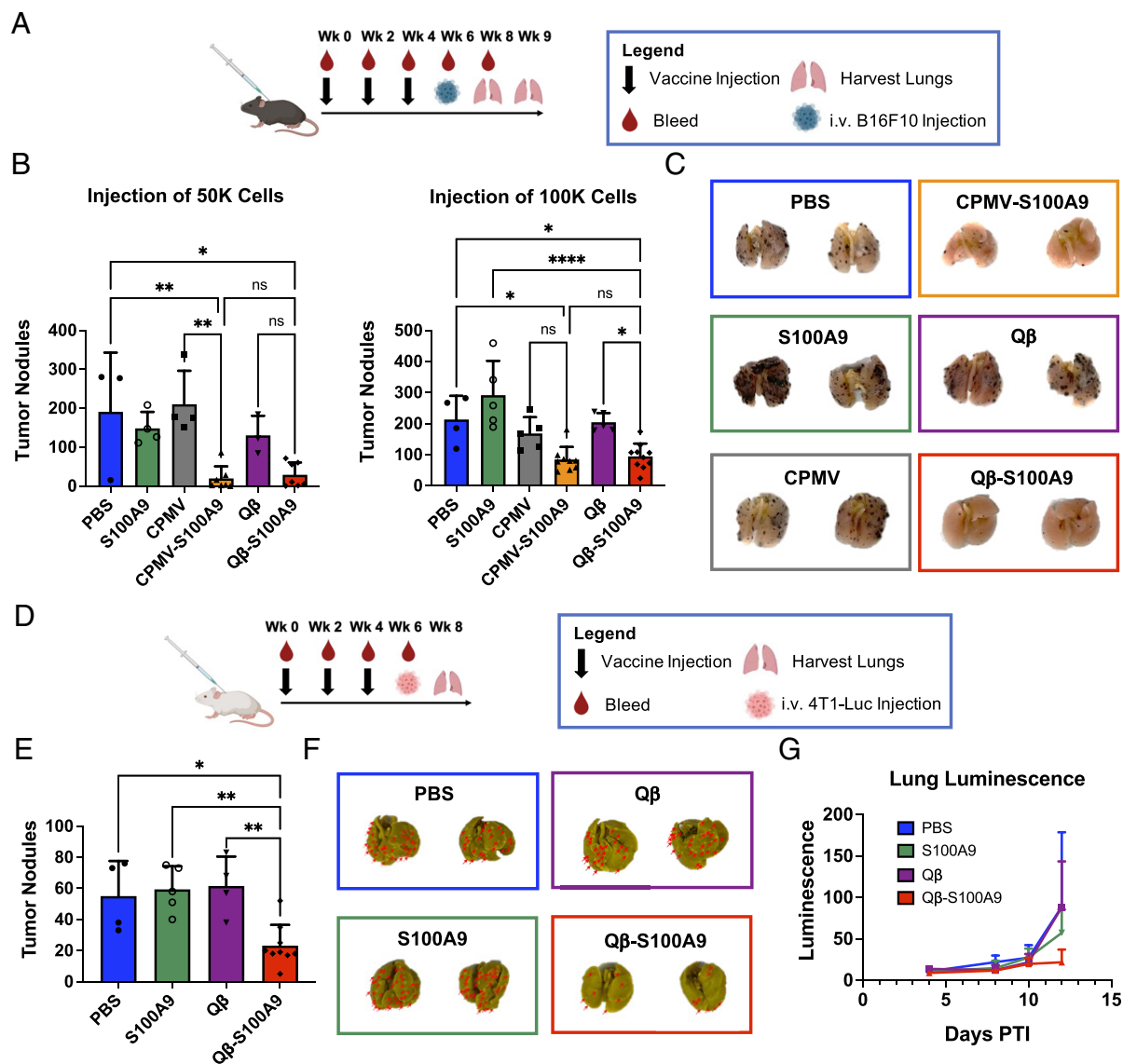
Fig. 3. Reduction of B16F10 and 4T1-Luc tumor nodules following vaccination. (*A*) Injection schedule in C57BL/6J mice. Lungs were harvested after 2 or 3 wk depending on the number of cells injected. (*B*) Quantitative analysis of B16F10 tumor nodules within the lungs (n = 3 to 10). Error bars represent the SD. (*C*) Qualitative images of the tumor nodules in *B*. The images are representative images of lungs from each group. The black dots on the lungs represent the B16F10 tumor nodules. (*D*) Injection schedule in BALB/C mice. (*E*) Quantitative analysis of the 4T1-Luc tumor nodules within the lungs (n = 4 to 10). Error bars represent the SD. (*F*) Representative images of lungs from *E*. The red arrows are pointing toward 4T1-Luc tumor nodules. The lungs are yellow due to the storing of the lungs in Bouin's solution to visualize 4T1-Luc tumor nodules. (*G*) Lung luminescence of mice from ROI measurements taken on the IVIS. Error bars represent the SD. The injection schedule schematics were created on Biorender.com. All analyses were done on GraphPad Prism, and the tumor nodules were compared using one-way ANOVA and Tukey's multiple comparisons test. $*P < 0.05$, $**P < 0.01$, $****P < 0.0001$, ns = not significant.

Next, we investigated Qβ-S100A9 efficacy using a 4T1-Luc TNBC model in BALB/c mice. Lungs were harvested 2 wk post-tumor challenge, and tumor nodules were counted after staining with Bouin's solution (Fig. 3 *D–F*). Again potent vaccine efficacy was observed, decreasing tumor nodule counts by 2.6-, 2.4-, and 2.6-fold compared to Qβ, PBS, and S100A9 peptide, respectively (Fig. 3 *E* and *F*). Weight measurements indicated no weight loss observed for the Qβ-S100A9 and S100A9 group; in contrast, PBS and Qβ mice lost weight drastically by day 8 (*SI Appendix*, Fig. S8). Tumor growth was measured using luminescence measurements on an in vivo imaging system (IVIS) and averaged region of interest (ROI) counts on the Living Image 3.0 software. Qβ-S100A9 vaccinated mice showed the slowest tumor growth, and by day 12, the luminescence within the lungs of the Qβ-S100A9 mice was 24.7, 24.5, and 38% of the Qβ, PBS, and S100A9 controls, respectively (Fig. 3*G*). The results from both the B16F10 and 4T1-Luc studies demonstrate that the vaccine

protects against tumor seeding within the lungs—in the clinic, we envision the vaccine working similarly in postsurgery patients with circulating tumor cells.

Qβ-S100A9 Vaccine Decreases Metastasis to the Lungs in TNBC Surgery Study. To investigate the ability of the vaccine in reducing metastasis, a 4T1-Luc primary tumor was injected s.c. prior to vaccination followed by surgery 2 wk after tumor implantation—metastasis to the lungs was examined *via* luminescent imaging. This experimental process mirrors clinical procedure, and it is known that 4T1-Luc cells begin to metastasize by day 16 (39). The treatment schedule is outlined in Fig. 4*A*. The lungs were imaged every 2 to 4 d following surgery, and the luminescence and survival of the mice were analyzed. In the control animals, tumors developed quickly following surgery, and by day 60, only 20% of the mice in the PBS and Qβ groups remained alive as well as 30% in the S100A9 group (Fig. 4*B*). On the other hand, 80% of the
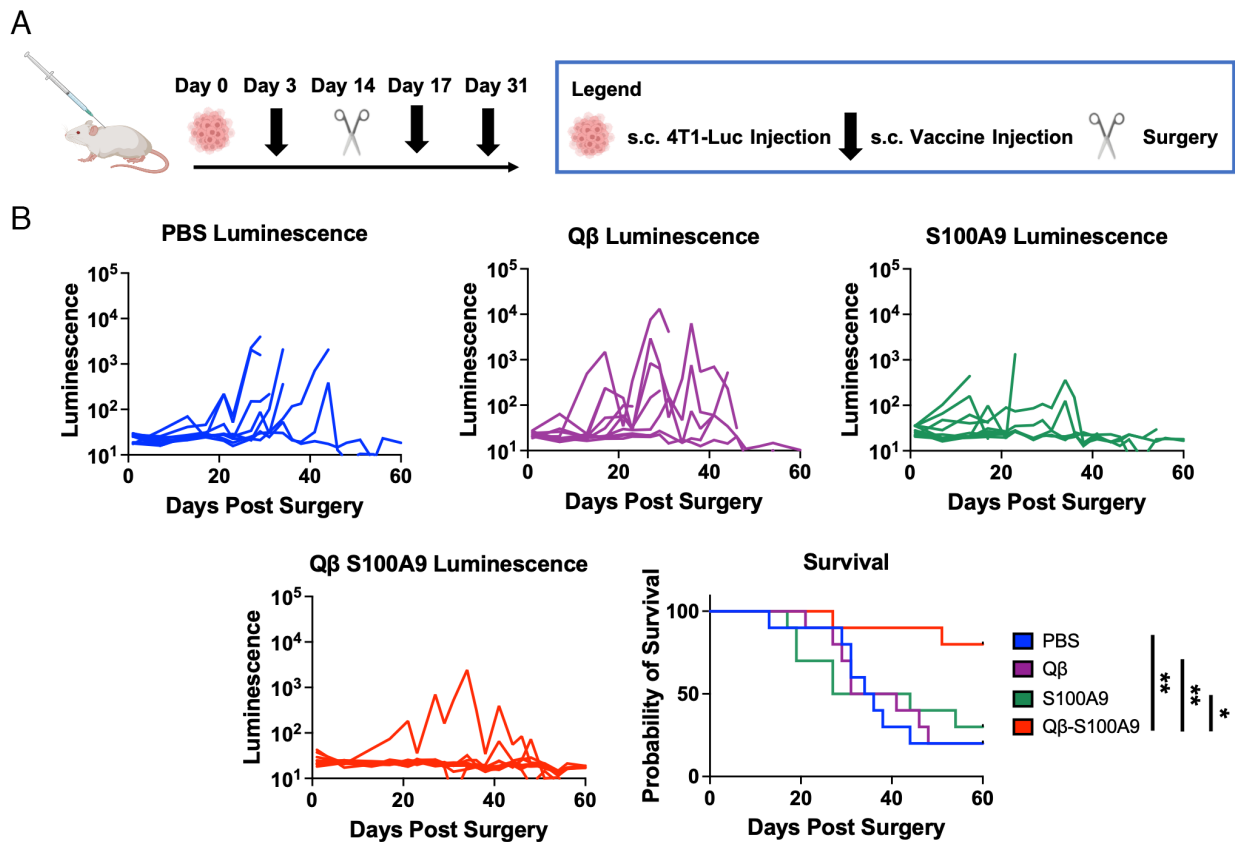
Fig. 4. Metastasis and recurrence study of surgically removed 4T1-Luc orthotopic tumors. (*A*) Injection schedule. The primary 4T1-Luc tumors were injected s.c. followed by surgical removal after 2 wk. The mice were then imaged every 2 to 4 d for onset of metastases or recurrences. (*B*) Luminescence of the 4T1-Luc tumors as measured by ROI measurements on the IVIS. The survival of the mice is also shown. In the tumor growth curves, the luminescence is shown on the *y* axis is log scale (n = 10). The injection schedule schematics were created on Biorender.com. All analyses were done on GraphPad Prism, and the survival was compared using the Log-rank (Mantel-Cox) test. *$P < 0.05$, **$P < 0.01$.

mice in the Qβ-S100A9 group remained alive and continued to be healthy until the last measured timepoint at day 60, indicating a survival improvement of 267 to 400% over controls. The survival curves and luminescent measurements indicate that the Qβ-S100A9 vaccine extends and improves survival in mice following surgical removal of TNBC due to the elimination of metastatic disease.

S100A8/9 Levels are Reduced in Lungs and Sera Following Vaccination. S100A8/9 levels in both the lungs and the sera were measured by the ELISA comparing vaccinated and unvaccinated, naive mice. We used S100A8/9 because S100A9 is typically found in the heterodimer form (9). Naive or vaccinated C57BL/6J mice were injected i.v. using 50,000 B16F10 cells; then, lungs and sera were collected pretumor challenge and 2 and 3 wk posttumor challenge (Fig. 5 *A, Top Left*).

In the naive mice, the S100A8/9 levels within the lungs remained similar before tumor challenge and 2 wk posttumor challenge (1,504 vs. 664 ng mL^{-1}); however, by week 3, there was a sudden 10× increase to 13,767 ng mL^{-1} (Fig. 5*B*). In stark contrast, in vaccinated mice, the S100A8/9 levels decreased in the lungs to 66.4 ng mL^{-1} prior to tumor injection, and even 2 and 3 wk following injection, the levels remained much lower at 182.2 and 360.3 ng mL^{-1}, respectively (Fig. 5*B*). Strikingly, the S100A8/9 levels within the lungs of vaccinated mice 3 wk posttumor injection were still lower than naive, unvaccinated mice showcasing the longitudinal ability of the vaccine to continuously lower S100A8/9 levels. The full ELISAs are shown in *SI Appendix,* Fig. S9. We did not observe

complete eradication of S100A8/9 within the lungs following vaccination, which may be a positive result given the central role of S100A8/9 in pathogenic clearance (59, 60). We did notice a trend toward increased bacterial load following vaccination (*SI Appendix,* Fig. S10), but additional safety studies should be carried out to pave the way for translational development of the cancer vaccine candidate. We note in our study that the slight increase in bacterial load did not seem to negatively impact the health of the mice, and even with potential side effects of vaccination, a significantly greater level of vaccinated mice survived tumor metastasis into the lungs (Fig. 4). This is in line with other works in which S100A9 was targeted by means of siRNA or small-molecule inhibitors (23, 61). It is also important to note that impaired immunity or increased infection rates were not noted as adverse effects in clinical trials of tasquinimod, which is a small-molecule inhibitor of S100A9 (62).

To ascertain that the decrease in the S100A8/9 in the lungs is not attributed to a decrease in tumor nodules, but more so the activity of the α-S100A9 antibodies, we also examined S100A8/9 levels in the sera. While systemic S100A8/9 levels fluctuate depending on disease state, S100A8/9 is mainly active locally, and decreases in systemic S100A8/9 should be mediated by vaccine-generated antibodies. By week 3 following B16F10 i.v. challenge, vaccinated groups showed trends toward decreased S100A8/9 sera levels compared to control animals (Fig. 5*C*). The 4T1-Luc data showed similar response to the vaccines with significant decreases in the lungs and trends in the sera of S100A8/9 (Fig. 5 *D* and *E*). The complete ELISAs are shown in *SI Appendix,* Fig. S11.

The lungs of both 4T1-Luc and B16F10-injected, vaccinated mice at the last measured time point (week 3 for B16F10, week 2 for
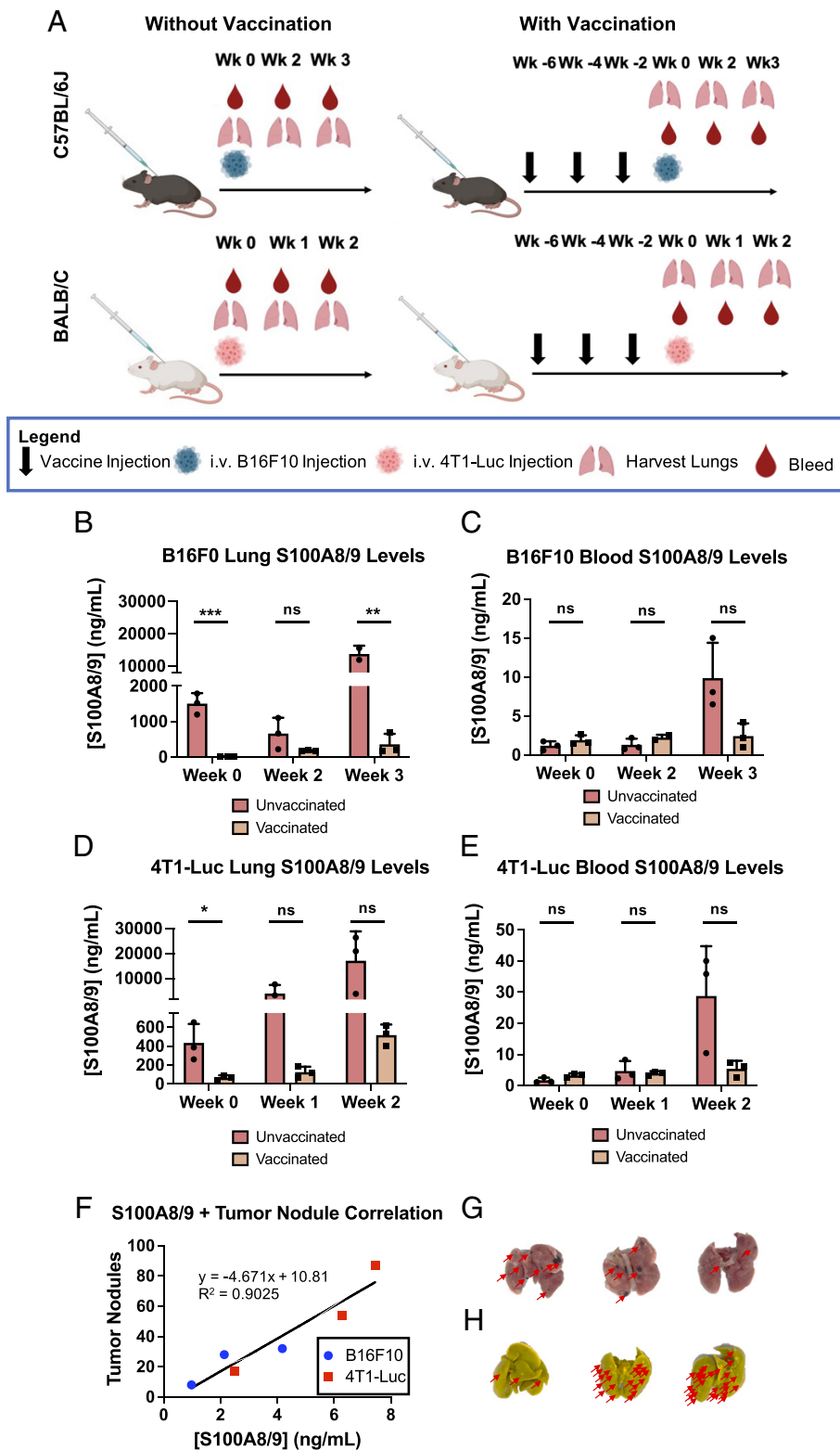
Fig. 5. S100A8/9 levels within the lungs and sera of B16F10- and 4T1-Luc-inoculated mice as a function of Qβ-S100A9 vaccination. (*A*) Injection and lung/sera collection schedule. (*B*) S100A8/9 levels in the lungs of C57BL/6J mice. (*C*) S100A8/9 levels in the sera of C57BL/6J mice. (*D*) S100A8/9 levels in the lungs of BALB/C mice. (*E*) S100A8/9 levels in the sera of BALB/C mice. (*F*) Scatter plot of mice comparing tumor nodule formation and S100A8/9 concentration within the sera. A line of best fit was plotted with an R^2 of 0.9025. (*G*) Tumor nodules within the lungs of B16F10-inoculated mice. The red arrows are pointing toward areas of tumor nodule formation. (*H*) Tumor nodules within the lungs of 4T1-Luc-inoculated mice. The red arrows are pointing toward areas of tumor nodule formation. All experiments were done with n = 2 to 3, and the error bars represent the SD. All statistics were accomplished with Student's *t* test. The injection schedule schematics were created on Biorender.com. *$P < 0.05$, **$P < 0.01$, ***$P < 0.001$, ns = not significant.

4T1-Luc) were then analyzed to investigate correlation between S100A8/9 sera levels and tumor nodule formation (Fig. 5 *F–H*). The sera of the mice were collected at the noted timepoints, and S100A8/9 levels were measured through ELISA and correlated to the number of tumor nodules. Indeed, mice with more tumor nodules also had elevated levels of S100A8/9. A line of best fit was calculated, which produced an R^2 of 0.9025. The correlation between S100A8/9 and tumor burden further validates that vaccination eliminates S100A8/9, leading to reduction of lung tumor nodules.

Cytokine and Immune Cell Analysis of Lungs Following Vaccination. S100A9 plays a direct immunomodulatory role on MDSCs by potentiating their immunosuppressive effects through both paracrine and autocrine functions, thereby promoting tumor growth (22). To gain insights into the mechanism of action of the Qβ-S100A9 vaccine candidate, we performed cytokine analysis using ELISAs on homogenized lungs (Fig. 6*A*). We focused on IL-10, IL-6, TGFβ, IFNγ, and IL-12, all of which are directly or indirectly related to MDSC function (63–67). Overall, for the

B16F10 mice, we noticed sharp decreases in immunosuppressive cytokines and an increase in immunostimulatory cytokines in Qβ-S100A9-vaccinated mice compared to unvaccinated mice (Fig. 6B). Before tumor injection, immunosuppressive cytokines IL-10 and TGFβ were decreased by 3.1- and 5.9-fold in vaccinated mice. These significant decreases continued into week 2 for IL-10 and into week 3 for TGFβ. The cytokine IL-6 was significantly increased 8.6-fold in vaccinated mice at week 0 (Fig. 6B). While IL-6 plays a role in upregulation of MDSCs (63), it also has known antitumoral effects

via simulating adaptive immunity and maturation of APCs (68, 69). Importantly, the immunostimulatory cytokines of IFNγ and IL-12 were strongly up-regulated in vaccinated mice. By the third week, IFNγ levels were 3.7-fold that of unvaccinated mice. IL-12 was not detectable by the ELISA in unvaccinated mice but was present in vaccinated mice at all timepoints. IFNγ and IL-12 both play crucial roles in creating an immunostimulatory, or "hot", TME (70–74). IL-12 directly regulates the antitumoral properties of natural killer cells and T cells, which go on to release IFNγ (70–72, 75). The
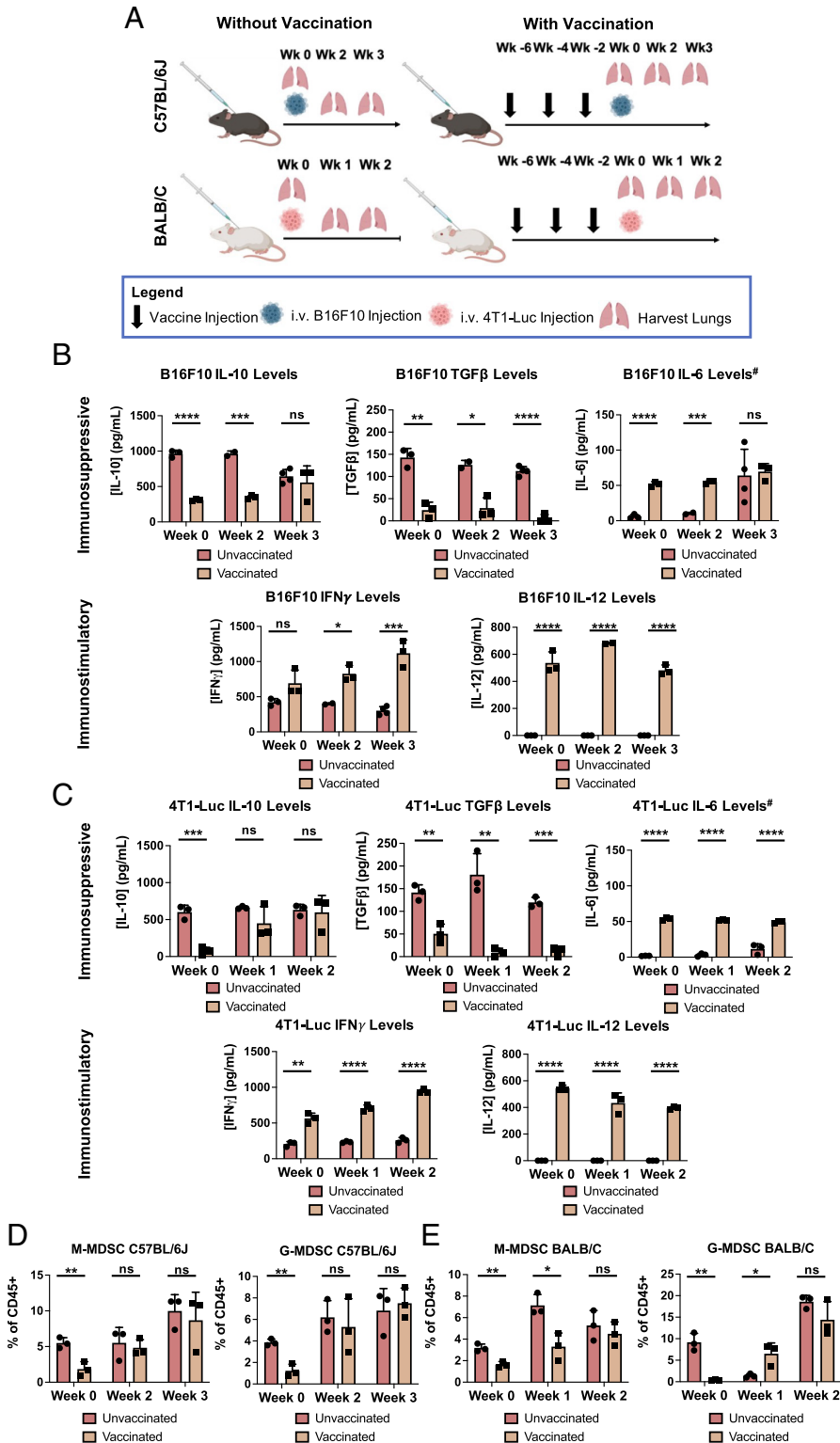
Fig. 6. Analysis of cytokine and MDSC levels within the lungs of B16F10- and 4T1-Luc-inoculated mice after Qβ-S100A9 vaccination. (A) Injection and lung harvesting schedule. (B) Concentration of IL-10, TGFβ, IL-6, IFNγ, and IL-12 in the lungs of vaccinated and naive C57BL/6J mice inoculated with B16F10 metastatic tumors. (C) Concentration of IL-10, TGFβ, IL-6, IFNγ, and IL-12 in the lungs of vaccinated and naive BALB/C mice inoculated with 4T1-Luc metastatic tumors. # IL-6 is listed as immunosuppressive, but also contributes to an immunostimulatory response. (D) M-MDSC and G-MDSC populations within the lungs of vaccinated and unvaccinated C57BL/6J mice inoculated with B16F10 tumors. (E) M-MDSC and G-MDSC populations within the lungs of vaccinated and unvaccinated BALB/C mice inoculated with 4T1-Luc tumors. All experiments were done with n = 2 to 4, and the analyses were run using Student's t test. The error bars represent the SD. *P < 0.05, **P < 0.01, ***P < 0.001, ****P < 0.0001, ns = not significant. The injection schedule schematics were created on Biorender.com.

IFNγ further activates Th1 effector mechanisms, which produces more IFNγ in a positive feedback loop. Downstream effects are increased differentiation of CD8+ T cells into effector cytotoxic T cells, leading to increased tumor cell killing and stimulation of systemic antitumoral immune memory (73, 74, 76). Overall, the trends in the 4T1-Luc mouse model were directly comparable with the B16F10 data in that the immunosuppressive cytokines IL-10 and TGFβ were decreased, while IL-6, IFNγ, and IL-12 were increased significantly (Fig. 6C). The cytokine analysis indicates that following vaccination of S100A9, there is an overall shift toward a more antitumor, immunostimulatory state, which most likely aids in the rejection of tumor nodule formation.

We also investigated the MDSC populations within the lungs as a function of vaccination against S100A9 (Fig. 6 D and E; see *SI Appendix*, Fig. S12 for the gating strategy) (77). Previous research has shown that decreasing S100A8/9 in both tumor-bearing and naive mice can diminish MDSC accumulation (22, 23), and our data corroborate these findings. In C57BL/6J mice, the population of monocytic MDSCs (M-MDSC) decreased by threefold, while the population of granulocytic MDSCs (G-MDSCs) was decreased 3.1-fold (Fig. 6D) at week 0. Similar trends were observed at week 0 in the 4T1-Luc model using BALB/C (Fig. 6E)—initially, there were significantly lower levels of G-MDSC and M-MDSC populations. We hypothesize that suppression of G-MDSCs and M-MDSCs in vaccinated mice helps to eliminate tumors at early onset before the tumors become difficult to eradicate. This is evidenced by the slower tumor growth in the 4T1-Luc-injected mice as seen through luminescent imaging (Fig. 3G). Additionally, the main source of S100A9 is attributed to G-MDSCs/neutrophils, and the sharp initial decline in G-MDSCs most likely contributes heavily to the decreased tumor seeding (Fig. 3) and metastasis (Fig. 4). Others have shown that G-MDSCs increase lung metastasis at a higher rate than M-MDSCs and that depleting G-MDSCs with an anti-Ly6G antibody prevents pulmonary metastasis of i.v.-injected EMT6 cells (78). Future experiments should investigate in further detail the innate immune cell changes outside of MDSCs, their inflammatory states (e.g., CD86 and MHC-II expression), and their differentiation following vaccination.

Together, data indicate two distinct mechanisms of action of the Qβ-S100A9 vaccine: 1) the reduction of S100A8/9 decreases tumor seeding into the lungs and 2) once seeded within the lungs, the tumors develop at slower rates due to the generation of a more antitumor, immunostimulatory environment. Prior research indicates that S100A8/9 recruits cancer cells into the lungs by increasing the expression of cytokines such as TGFβ (26). Therefore, reducing S100A8/9 and TGFβ levels synergistically blocks lung metastasis (Figs. 5 B and D and 6 B and C). Our data are consistent with a report showing that B16F10 cells home to the lungs of uteroglobin knockout (KO) mice which highly express S100A9 within the lungs (79). Blocking the interaction of S100A9 with B16F10 using antibodies led to decreased metastasis and invasion of the B16F10 cells. An advantage of our vaccine (active immunotherapy) over antibody treatment (passive immunotherapy) is that such therapies will require continuous intervention. By creating a vaccine, the patient will be able to synthesize their own antibodies against S100A9, and continuous drugging may not be necessary, therefore improving quality of life and reducing costs. This additionally pertains to small-molecule inhibitors such as tasquinimod, which need to be dosed daily for up to 2 wk (80, 81).

Another facet of S100A9 is that it promotes MDSC accumulation in both naive and tumor-bearing mice (22, 23). By vaccinating against S100A9, the initial M-MDSC and G-MDSC populations are decreased, (Fig. 6 D and E) most likely decreasing tumor seeding and growth. In S100A9 KO mice, 9 of 12 implanted tumors were rejected in a lymphoma model due to decreased MDSC populations, while the tumors grew aggressively in WT mice (23). Similar reports have been shown in numerous other cancer models (21, 22, 79, 82–84). MDSCs are also potent producers of IL-10 and TGFβ (70), and our data clearly indicate that along with diminished MDSC populations, the concentration of immunosuppressive cytokines is decreased following vaccination (Fig. 6 B and C). In the TME, IL-10 and TGFβ act on dendritic cells and M1 macrophages restricting their production of IL-12, which acts on natural killer cells to promote antitumor immunity (70–72). The downstream effects are that IFNγ production and thereby CD8+ T cell activity and tumor cell killing are decreased (73, 74). Indeed, in both the B16F10 and 4T1-Luc models, IL-10 and TGFβ are significantly up-regulated in unvaccinated mice, while IFNγ and IL-12 become down-regulated (Fig. 6 B and C)—vaccination helps to reverse this effect. The flow cytometry data coupled with the cytokine analysis help to validate that vaccination works to negate the effects of the MDSC populations within the lungs, thereby reducing metastasis/tumor seeding and growth of the injected tumors.

Last, while not explored in the current work, S100A9 has been implicated in metastasis and recurrence within other major organs of metastasis such as the liver, bone marrow, and brain (85–88). Therefore, we envision that the vaccine could be expanded to prevent metastatic outgrowths in organs outside of the lungs and in other cancer types outside of melanoma and TNBC.

Conclusion

The data indicate that vaccination against S100A9 utilizing CPMV and Qβ as an adjuvant and display platform can prime the immune system to reduce S100A9 levels pre- and posttumor challenge. This leads to reprogramming of the premetastatic niche and TME and protection from tumor challenge of melanoma and TNBC. Immunization using Qβ-S100A9 and CPMV-S100A9 induced high titers of α-S100A9 antibodies with Qβ-S100A9 generating higher titers than CPMV-S100A9. Safety of the vaccine candidates is indicated as cross-reactivity to S100A8 was not apparent. Potent efficacy was demonstrated in mouse models of melanoma and TNBC with dramatic reduction of tumor nodules and delayed onset of tumor growth. A clinically relevant primary tumor surgery model also showcased improved survival in vaccinated mice. Mechanism studies revealed reduced S100A8/9 levels in the lungs and sera, changes in cytokine profiles skewing toward an antitumor, immunostimulatory TME along with suppression of MDSCs. In summary, the CPMV and Qβ-S100A9 vaccines demonstrate significant efficacy in reducing the onset of metastatic outgrowths to the lungs of melanoma and TNBC and warrant further investigation into its use as a vaccine platform against metastatic cancers.

Materials and Methods

Preparation of S100A9-Subunit Vaccines. CPMV nanoparticles were propagated in black-eyed pea No. 5 plants and purified as previously reported (45). Qβ VLPs were expressed in Bl21 (DE3) (New England BioLabs) and purified as previously reported (38).

CPMV and Qβ were first conjugated to a heterobifunctional linker, SM(PEG)$_8$, for 2 h followed by ultracentrifugation at 52,000 g for 1 h at 4 °C. The S100A9 peptide (sequence: CGSGRGHGHSHGKG) was reacted with the viruses for 2 h at RT and then purified using a 12 to 14 kDa molecular weight cut off (MWCO) dialysis membrane (Avantor) in 10 mM KP.

Characterization of CPMV-S100A9 and Qβ-S100A9 Particles. The CPMV and Qβ-S100A9 particles were characterized by UV-VIS, SDS-PAGE, agarose gel electrophoresis, TEM, SEC, and DLS as done previously (89).

Animal Immunization. C57BL/6J mice were injected 3× s.c. spaced 2 wk apart with 200 μg of CPMV, CPMV-S100A9, Qβ, Qβ-S100A9, PBS, and the S100A9 peptide. Two weeks after the last dose, the mice were injected i.v. with either 50,000 or 100,000 B16F10 melanoma cells. The sera from the mice were collected every 2 wk from week 2 to week 8.

BALB/C mice received the same dosing regimen as with the C57BL/6J mice with the exception that only the Qβ, Qβ-S100A9, and S100A9 peptide groups were tested. At week 6, 50,000 4T1-Luc cells were injected i.v., and sera were collected every 2 wk until week 8.

Antibody Titers against S100A9 Peptide and VNP/VLPs. ELISA was performed against the S100A9 peptide using maleimide-activated plates (Thermo Fisher Scientific) according to the manufacturer's instructions. The CPMV and Qβ-S100A9 groups were further analyzed for antibody isotyping against IgG$_{total}$, IgG1, IgG2a, IgG2b, IgG2c, IgA, IgM, and IgE.

For antibody titers against the viral carriers, CPMV or Qβ were coated on Microlon 200 plates (Greiner Bio-One) overnight at 4 °C and examined by ELISA like above.

WB and DBs against Full-Length S100A8 and S100A9. WB and DBs against both S100A9 and S100A8 were carried out. SDS-PAGE gels were transferred onto nitrocellulose paper (VWR), and blocked with 10% (w/v) skim milk. The sera at the week 6 timepoint were pooled from the CPMV-S100A9, Qβ-S100A9, and S100A9 peptide-only samples and incubated for 1 h at RT. Following binding with a goat anti-mouse HRP secondary antibody for 1 h, a 3,3′-diaminobenzidine substrate was added for 2 min and washed away. The blots were then imaged on an AlphaImager system. For the DBs, the S100A8 and S100A9 proteins were directly added to the nitrocellulose paper before analysis like the WB.

Lung Tumor Seeding B16F10 and 4T1-Luc Model. Naive and vaccinated mice were challenged i.v. with B16F10 and 4T1-Luc cells as in *Animal Immunization*. C57BL/6J mice lungs were harvested after 2 or 3 wk (depending on injection of 50,000 vs. 100,000 cells, respectively) and stored in 10% (v/v) neutral-buffered formalin (Sigma-Aldrich) followed by 70% (v/v) EtOH. The tumor nodules were then manually counted. BALB/C mice injected with 4T1-Luc were analyzed via luminescence imaging using an IVIS (Xenogen). The mice were injected intraperitoneally with 150 mg kg^{-1} and luminescence was measured using ROI measurements. The lungs were collected after 2 wk and stored in Bouin's solution (Sigma-Aldrich) followed by 70% (v/v) EtOH.

4T1-Luc Primary Cancer Surgical Removal Metastasis Study. BALB/C mice were injected s.c. in the left flank with 200,000 4T1-Luc cells in 100 μL of PBS. Three days following tumor inoculation, the mice were vaccinated with either PBS, Qβ, S100A9 peptide only, or Qβ-S100A9 (200 μg mouse^{-1}) as described in *Animal Immunization*. Fourteen days PTI, the s.c. tumors were surgically removed, and the skin was sutured using Vetbond tissue adhesive (3M). The vaccine regimen was completed following surgery at 2-wk intervals as described above. The mice were subjected to luminescence imaging as in *Lung Tumor Seeding B16F10 and 4T1-Luc*

Model, and ROI measurements were taken to assess lung metastasis and tumor recurrence

S100A8/9 Levels in the Lungs and Serum Following Vaccination. S100A8/9 levels within the lungs and sera were analyzed using a mouse S100A8/9 detection kit (research and development (R&D) Systems) according to the manufacturer's instructions. Prior to the ELISAs, the lungs were harvested at weeks 0, 1, and 3 (in C57BL/6J mice) and weeks 0, 1, and 2 (in BALB/C mice) in both vaccinated and naive mice and homogenized using a LabGEN 125 homogenizer (Cole-Parmer). Analysis of sera was accomplished through sera collected through r.o. bleeding in both vaccinated and naive mice at the same timepoints.

Cytokine Analysis of Lungs. The lungs of both vaccinated and unvaccinated BALB/C and C57BL/6J mice were analyzed for expression of IL-6, IL-10, IL-12, TGFβ, and IFNγ through ELISA (ThermoFisher) according to the manufacturer's instructions. The lungs were collected at the same timepoints as in *S100A8/9 Levels in the Lungs and Serum Following Vaccination*, and homogenized and dissociated in tissue extraction reagent II (ThermoFisher) supplemented with a protease inhibitor cocktail (ThermoFisher) and 10 mM PMSF.

Flow Cytometry of Lungs. The lungs of both vaccinated and unvaccinated BALB/C and C57BL/6J mice were collected as before and dissociated into single-cell suspensions using a lung dissociation kit (Militenyi Biotec) according to the manufacturer's instructions. The cells were stained with LIVE/DEAD Aqua (Thermo Scientific) and blocked with 1 μg mL^{-1} of an Fc block solution (BioLegend). The cells were then stained with the following antibodies (BioLegend): Pacific Blue CD45, SuperBright 645-CD11b, PE-eFluor610-Ly6G, and PE/Cy7-Ly6C. Flow cytometry was done using a BD FACSCelesta and data analysis was done using FlowJo.

Statistical Analysis. All analyses were done on GraphPad Prism. The tumor nodule counts were compared using one-way ANOVA. S100A8/9 levels, cytokine levels, and MDSC populations were analyzed using Student's *t* test. All error bars represent the SD.

Author affiliations: [a]Department of Bioengineering, University of California, San Diego, CA 92093; [b]Moores Cancer Center, University of California, San Diego, CA 92093; [c]Department of NanoEngineering, University of California, San Diego, CA 92093; [d]Department of Radiology, University of California, San Diego, CA 92093; [e]Institute for Materials Discovery and Design, University of California, San Diego, CA 92093; [f]Center for Nano-ImmunoEngineering, University of California, San Diego, CA 92093; and [g]Center for Engineering in Cancer, University of California, San Diego, CA 92093

1. A. Wells, J. Grahovac, S. Wheeler, B. Ma, D. Lauffenburger, Targeting tumor cell motility as a strategy against invasion and metastasis. *Trends Pharmacol. Sci.* **34**, 283–289 (2013).
2. X. Guan, Cancer metastases: Challenges and opportunities. *Acta Pharm. Sin. B* **5**, 402–418 (2015).
3. O. Peart, Metastatic breast cancer. *Radiol. Technol.* **88**, 519M–539M (2017).
4. L. Enewold, E. Sharon, L. C. Harlan, Metastatic melanoma: Treatment and survival in the US after the introduction of ipilimumab and vemurafenib. *Oncol. Res. Treat.* **40**, 174–183 (2017).
5. S. Zhang, Y. Wang, Y. Ding, Y. Wu, Long term survival results in advanced prostate cancer treated with combined androgen blockade. *Zhonghua Nan Ke Xue.* **11**, 770–771, 774 (2005).
6. A. B. Gardner *et al.*, Ovarian, uterine, and cervical cancer patients with distant metastases at diagnosis: Most common locations and outcomes. *Clin. Exp. Metastasis* **37**, 107–113 (2020).
7. A. Jamil, A. Kasi, "lung metastasis" in *StatPearls* (StatPearls Publishing, 2022) (24 May 2022).
8. G. Srikrishna, S100A8 and S100A9: New insights into their roles in malignancy. *J. Innate Immun.* **4**, 31–40 (2011).
9. S. Wang *et al.*, S100A8/A9 in inflammation. *Front. Immunol.* **9**, 1298 (2018).
10. K. Croce *et al.*, MRP-8/14 is critical for the biological response to vascular injury. *Circulation* **120**, 427–436 (2009).
11. C. Gebhardt, J. Németh, P. Angel, J. Hess, S100A8 and S100A9 in inflammation and cancer. *Biochem. Pharmacol.* **72**, 1622–1631 (2006).
12. I. Salama, P. S. Malone, F. Mihaimeed, J. L. Jones, A review of the S100 proteins in cancer. *Eur. J. Surg. Oncol.* **34**, 357–364 (2008).
13. H. M. Koh *et al.*, Prognostic role of S100A9 expression in patients with clear cell renal cell carcinoma. *Medicine (Baltimore)* **98**, e17188 (2019).
14. J. Liao *et al.*, High S100A9$^+$ cell density predicts a poor prognosis in hepatocellular carcinoma patients after curative resection. *Aging (Albany NY)* **13**, 16367–16380 (2021).
15. J. Meng, F. Gu, H. Fang, B. Qu, Elevated serum S100A9 indicated poor prognosis after hepatocellular carcinoma after curative resection. *J. Cancer* **10**, 408–415 (2019).
16. Z. Lv, W. Li, X. Wei, S100A9 promotes prostate cancer cell invasion by activating TLR4/NF-κB/integrin β1/FAK signaling. *Onco Targets Ther.* **13**, 6443–6452 (2020).
17. R. Song, K. Struhl, S100A8/S100A9 cytokine acts as a transcriptional coactivator during breast cellular transformation. *Sci. Adv.* **7**, eabe5357 (2021).
18. W.-Y. Fang *et al.*, Elevated S100A9 expression in tumor stroma functions as an early recurrence marker for early-stage oral cancer patients through increased tumor cell invasion, angiogenesis, macrophage recruitment and interleukin-6 production. *Oncotarget* **6**, 28401–28424 (2015).
19. K. Arai *et al.*, S100A8 and S100A9 overexpression is associated with poor pathological parameters in invasive ductal carcinoma of the breast. *Curr. Cancer Drug Targets* **8**, 243–252 (2008).
20. C. Zhao *et al.*, S100A9 regulates cisplatin chemosensitivity of squamous cervical cancer cells and related mechanism. *Cancer Manag. Res.* **10**, 3753–3764 (2018).
21. J. Li *et al.*, S100A9-CXCL12 activation in BRCA1-mutant breast cancer promotes an immunosuppressive microenvironment associated with resistance to immunotherapy. *Nat. Commun.* **13**, 1481 (2022).
22. P. Sinha *et al.*, Proinflammatory S100 proteins regulate the accumulation of myeloid-derived suppressor cells. *J. Immunol.* **181**, 4666–4675 (2008).
23. P. Cheng *et al.*, Inhibition of dendritic cell differentiation and accumulation of myeloid-derived suppressor cells in cancer is regulated by S100A9 protein. *J. Exp. Med.* **205**, 2235–2249 (2008).

24. O. Turovskaya et al., RAGE, carboxylated glycans and S100A8/A9 play essential roles in colitis-associated carcinogenesis. *Carcinogenesis* **29**, 2035–2043 (2008).

25. P. Goedegebuure et al., Myeloid-derived suppressor cells: General characteristics and relevance to clinical management of pancreatic cancer. *Curr. Cancer Drug Targets* **11**, 734–751 (2011).

26. S. Hiratsuka, A. Watanabe, H. Aburatani, Y. Maru, Tumour-mediated upregulation of chemoattractants and recruitment of myeloid cells predetermines lung metastasis. *Nat. Cell Biol.* **8**, 1369–1375 (2006).

27. University of Pennsylvania, Phase 1 study of tasquinimod alone and in combination with standard therapy for relapsed or refractory myeloma. (2022). clinicaltrials.gov. 9 November 2022.

28. A. Moon et al., Global gene expression profiling unveils S100A8/A9 as candidate markers in H-ras-mediated human breast epithelial cell invasion. *Mol. Cancer Res.* **6**, 1544–1553 (2008).

29. H.-Y. Yong, A. Moon, Roles of calcium-binding proteins, S100A8 and S100A9, in invasive phenotype of human gastric cancer cells. *Arch. Pharm. Res.* **30**, 75–81 (2007).

30. M. O. Mohsen, G. Augusto, M. F. Bachmann, The 3Ds in virus-like particle based-vaccines: "Design, delivery and dynamics". *Immunol. Rev.* **296**, 155–168 (2020).

31. Y. H. Chung et al., Integrating plant molecular farming and materials research for next-generation vaccines. *Nat. Rev. Mater.* **7**, 372–388 (2021).

32. G. Spohn et al., A virus-like particle-based vaccine selectively targeting soluble TNF-α protects from arthritis without inducing reactivation of latent tuberculosis. *J. Immunol.* **178**, 7450–7457 (2007).

33. M. F. Bachmann, M. R. Dyer, Therapeutic vaccination for chronic diseases: A new class of drugs in sight. *Nat. Rev. Drug Discov.* **3**, 81–88 (2004).

34. C. I. Nkanga, O. A. Ortega-Rivera, M. D. Shin, M. A. Moreno-Gonzalez, N. F. Steinmetz, Injectable slow-release hydrogel formulation of a plant virus-based COVID-19 vaccine candidate. *Biomacromolecules* **23**, 1812–1825 (2022).

35. S. Ray, D. M. Wirth, O. A. Ortega-Rivera, N. F. Steinmetz, J. K. Pokorski, Dissolving microneedle delivery of a prophylactic HPV vaccine. *Biomacromolecules* **23**, 903–912 (2022).

36. O. A. Ortega-Rivera et al., Cowpea mosaic virus nanoparticle vaccine candidates displaying peptide epitopes can neutralize the severe acute respiratory syndrome coronavirus. *ACS Infect. Dis.* **7**, 3096–3110 (2021).

37. O. A. Ortega-Rivera et al., Trivalent subunit vaccine candidates for COVID-19 and their delivery devices. *J. Am. Chem. Soc.* **143**, 14748–14765 (2021).

38. O. A. Ortega-Rivera, J. K. Pokorski, N. F. Steinmetz, A Single-Dose, Implant-based, trivalent virus-like particle vaccine against "cholesterol checkpoint" proteins. *Adv. Ther. (Weinh)* **4**, 2100014 (2021).

39. P. H. Lizotte et al., In situ vaccination with Cowpea mosaic virus nanoparticles suppresses metastatic cancer. *Nat. Nanotechnol.* **11**, 295–303 (2016).

40. T. Kawano et al., Therapeutic vaccine against S100A9 (S100 Calcium-Binding Protein A9) inhibits thrombosis without increasing the risk of bleeding in ischemic stroke in mice. *Hypertension* **72**, 1355–1364 (2018).

41. M. C. Jespersen, B. Peters, M. Nielsen, P. Marcatili, BepiPred-2.0: Improving sequence-based B-cell epitope prediction using conformational epitopes. *Nucleic Acids Res.* **45**, W24–W29 (2017).

42. W. Nacken, C. Sopalla, C. Pröpper, C. Sorg, C. Kerkhoff, Biochemical characterization of the murine S100A9 (MRP14) protein suggests that it is functionally equivalent to its human counterpart despite its low degree of sequence homology. *Eur. J. Biochem.* **267**, 560–565 (2000).

43. O. A. Ortega-Rivera, M. D. Shin, M. A. Moreno-Gonzalez, J. K. Pokorski, N. F. Steinmetz, A single-dose Qβ VLP vaccine against S100A9 protein reduces atherosclerosis in a preclinical model. *Adv. Ther. (Weinh)* **5**, 2200092 (2022).

44. V. P. Reddy Chichili, V. Kumar, J. Sivaraman, Linkers in the structural biology of protein–protein interactions. *Protein Sci.* **22**, 153–167 (2013).

45. A. M. Wen et al., Viral nanoparticles for in vivo tumor imaging. *J. Vis. Exp.*, **69**, e4352 (2012).

46. S. Shukla et al., The unique potency of Cowpea mosaic virus (CPMV) in situ cancer vaccine. *Biomater. Sci.* **8**, 5489–5503 (2020).

47. D. J. K. Pokorski, M. L. Hovlid, P. M. G. Finn, Cell targeting with hybrid Qβ virus-like particles displaying epidermal growth factor. *Chembiochem* **12**, 2441 (2011).

48. A. Shahrivarkevishahi et al., PhotothermalPhage: A virus-based photothermal therapeutic agent. *J. Am. Chem. Soc.* **143**, 16428–16438 (2021).

49. S. Nazeri, S. Zakeri, A. A. Mehrizi, S. Sardari, N. D. Djadid, Measuring of IgG2c isotype instead of IgG2a in immunized C57BL/6 mice with plasmodium vivax TRAP as a subunit vaccine candidate in order to correct interpretation of Th1 versus Th2 immune response. *Exp. Parasitol.* **216**, 107944 (2020).

50. C. Mao, V. Beiss, J. Fields, N. F. Steinmetz, S. Fiering, Cowpea mosaic virus stimulates antitumor immunity through recognition by multiple MYD88-dependent toll-like receptors. *Biomaterials* **275**, 120914 (2021).

51. S. Schulte, G. K. Sukhova, P. Libby, Genetically programmed biases in Th1 and Th2 immune responses modulate atherogenesis. *Am. J. Pathol.* **172**, 1500–1508 (2008).

52. J.-W. Lim et al., Co-delivery of antigens and immunostimulants via a polymersome for improvement of antigen-specific immune response. *J. Mater. Chem. B* **8**, 5620–5626 (2020).

53. Y. H. Chung, B. A. Volckaert, N. F. Steinmetz, Development of a modular NTA: His tag viral vaccine for co-delivery of antigen and adjuvant. *Bioconjug. Chem.* **34**, 269–278 (2023).

54. D. S. Watson, V. M. Platt, L. Cao, V. J. Venditto, F. C. Szoka, Antibody response to polyhistidine-tagged peptide and protein antigens attached to liposomes via lipid-linked nitrilotriacetic acid in mice. *Clin. Vaccine Immunol.* **18**, 289–297 (2011).

55. Z. Zhao, O. A. Ortega-Rivera, Y. H. Chung, A. Simms, N. F. Steinmetz, A co-formulated vaccine of irradiated cancer cells and cowpea mosaic virus improves ovarian cancer rejection. *J. Mater. Chem. B* **11**, 5429–5441 (2023), 10.1039/d2tb02355e.

56. C. D. Lemke-Miltner et al., Antibody opsonization of a TLR9-agonist-containing virus-like particle enhances in situ immunization. *J. Immunol.* **204**, 1386–1394 (2020).

57. Checkmate Pharmaceuticals, A multicenter, open-label, phase 2 study of intratumoral CMP-001 in combination with an intravenous PD-1-blocking antibody in subjects with selected types of advanced or metastatic cancer. (2022). clinicaltrials.gov. 24 May 2022.

58. Checkmate Pharmaceuticals, A multicenter, phase 2, open-label study of intratumoral CMP-001 in combination with intravenous pembrolizumab in subjects with recurrent or metastatic head and neck squamous cell carcinoma. (2022). clinicaltrials.gov. 24 May 2022.

59. H. L. Clark et al., Zinc and manganese chelation by neutrophil S100A8/A9 (Calprotectin) limits extracellular aspergillus fumigatus hyphal growth and corneal infection. *J. Immunol.* **196**, 336–344 (2016).

60. C. F. Urban et al., Neutrophil extracellular traps contain calprotectin, a cytosolic protein complex involved in host defense against Candida albicans. *PLoS Pathog.* **5**, e1000639 (2009).

61. Y. Li et al., S100a8/a9 signaling causes mitochondrial dysfunction and cardiomyocyte death in response to ischemic/reperfusion injury. *Circulation* **140**, 751–764 (2019).

62. N. Gupta, O. Al Ustwani, L. Shen, R. Pili, Mechanism of action and clinical activity of tasquinimod in castrate-resistant prostate cancer. *Onco Targets Ther.* **7**, 223–234 (2014).

63. R. Weber et al., IL-6 as a major regulator of MDSC activity and possible target for cancer immunotherapy. *Cell. Immunol.* **359**, 104254 (2021).

64. J. F. Santibanez, S. Bjelica, Transforming growth factor-beta1 and myeloid-derived suppressor cells interplay in cancer. *Open Cancer Immunol. J.* **6**, 1–14 (2017).

65. D. Jorgovanovic, M. Song, L. Wang, Y. Zhang, Roles of IFN-γ in tumor progression and regression: A review. *Biomark. Res.* **8**, 49 (2020).

66. C. E. Steding et al., The role of interleukin-12 on modulating myeloid-derived suppressor cells, increasing overall survival and reducing metastasis. *Immunology* **133**, 221–238 (2011).

67. K. Hart, K. Byrne, M. Molloy, E. Usherwood, B. Berwin, IL-10 immunomodulation of myeloid cells regulates a murine model of ovarian cancer. *Front. Immunol.* **2**, 29 (2011).

68. C. Wang, S. N. Fiering, N. F. Steinmetz, Cowpea Mosaic Virus promotes anti-tumor activity and immune memory in a mouse ovarian tumor model. *Adv. Ther. (Weinh)* **2**, 1900003 (2019).

69. F. Martinon, A. Mayor, J. Tschopp, The inflammasomes: Guardians of the body. *Annu. Rev. Immunol.* **27**, 229–265 (2009).

70. M. M. Yaseen, N. M. Abuharfeil, H. Darmani, A. Daoud, Mechanisms of immune suppression by myeloid-derived suppressor cells: The role of interleukin-10 as a key immunoregulatory cytokine. *Open Biol.* **10**, 200111 (2020).

71. C.-E. Hu, J. Gan, R.-D. Zhang, Y.-R. Cheng, G.-J. Huang, Up-regulated myeloid-derived suppressor cell contributes to hepatocellular carcinoma development by impairing dendritic cell function. *Scand. J. Gastroenterol.* **46**, 156–164 (2011).

72. M. A. Y. Alqudah, M. M. M. Yaseen, M. M. S. Yaseen, HIV-1 strategies to overcome the immune system by evading and invading innate immune system. *HIV AIDS Rev.* **15**, 1–12 (2016).

73. M. R. Porembka et al., Pancreatic adenocarcinoma induces bone marrow mobilization of myeloid-derived suppressor cells which promote primary tumor growth. *Cancer Immunol. Immunother.* **61**, 1373–1385 (2012).

74. G. Li et al., Vasoactive intestinal peptide induces CD14+HLA-DR-/low myeloid-derived suppressor cells in gastric cancer. *Mol. Med. Rep.* **12**, 760–768 (2015).

75. R. Parihar, J. Dierksheide, Y. Hu, W. E. Carson, IL-12 enhances the natural killer cell cytokine response to Ab-coated tumor cells. *J. Clin. Invest.* **110**, 983–992 (2002).

76. F. Castro, A. P. Cardoso, R. M. Gonçalves, K. Serre, M. J. Oliveira, Interferon-gamma at the crossroads of tumor immune surveillance or evasion. *Front. Immunol.* **9**, 847 (2018).

77. V. Bronte et al., Recommendations for myeloid-derived suppressor cell nomenclature and characterization standards. *Nat. Commun.* **7**, 12150 (2016).

78. M. Ouzounova et al., Monocytic and granulocytic myeloid derived suppressor cells differentially regulate spatiotemporal tumour plasticity during metastatic cascade. *Nat. Commun.* **8**, 14979 (2017).

79. A. Saha et al., Lack of an endogenous anti-inflammatory protein in mice enhances colonization of B16F10 melanoma cells in the lungs. *J. Biol. Chem.* **285**, 10822–10831 (2010).

80. C. Sternberg et al., Randomized, double-blind, placebo-controlled phase III study of tasquinimod in men with metastatic castration-resistant prostate cancer. *J. Clin. Oncol.* **34**, 2636–2643 (2016).

81. Active Biotech AB, A phase 3 randomized, double-blind, placebo-controlled study of tasquinimod in men with metastatic castrate resistant prostate cancer. (2015). clinicaltrials.gov. 9 November 2022.

82. H. Qin et al., Generation of a novel therapeutic peptide that depletes MDSC in tumor-bearing mice. *Nat. Med.* **20**, 676–681 (2014).

83. E. McNeill, N. Hogg, S100A9 has a protective role in inflammation-induced skin carcinogenesis. *Int. J. Cancer* **135**, 798–808 (2014).

84. S. Cheng et al., Down-regulation of S100A9 inhibits osteosarcoma cell growth through inactivating MAPK and NF-κB signaling pathways. *BMC Cancer* **16**, 253 (2016).

85. L. Duan et al., HBx-induced S100A9 in NF-κB dependent manner promotes growth and metastasis of hepatocellular carcinoma cells. *Cell Death Dis.* **9**, 1–14 (2018).

86. J. Meng, F. Gu, H. Fang, B. Qu, Elevated serum S100A9 indicated poor prognosis in hepatocellular carcinoma after curative resection. *J. Cancer* **10**, 408–415 (2019).

87. C. Monteiro et al., Stratification of radiosensitive brain metastases based on an actionable S100A9/RAGE resistance mechanism. *Nat. Med.* **28**, 752–765 (2022).

88. F. Morandi et al., Bone marrow-infiltrating human neuroblastoma cells express high levels of calprotectin and HLA-G proteins. *PLoS One* **7**, e29922 (2012).

89. Y. H. Chung, J. Park, H. Cai, N. F. Steinmetz, S100A9-targeted Cowpea Mosaic virus as a prophylactic and therapeutic immunotherapy against metastatic breast cancer and melanoma. *Adv. Sci.* **8**, e2101796 (2021).

90. N. F. Steinmetz, CPMV-S100A9. caNanoLab. https://cananolab.cancer.gov/#/home/samples/view-sample/115900491. Deposited 27 September 2023.

91. N. F. Steinmetz, Qbeta-S100A9. caNanoLab. https://cananolab.cancer.gov/#/home/samples/view-sample/115900492. Deposited 28 September 2023.